Coherent band-edge oscillations and dynamic longitudinal-optical phonon mode splitting as evidence for polarons in perovskites

Z. Liu,[1] C. Vaswani,[1] L. Luo,[1] D. Cheng,[1] X. Yang,[1] X. Zhao,[1] Y. Yao,[1] Z. Song,[2] R. Brenes,[3] R. J. H. Kim,[1] J. Jean,[3] V. Bulović,[3] Y. Yan,[2] K.-M. Ho,[1] and J. Wang[1,*]

[1]*Department of Physics and Astronomy, Ames Laboratory, Iowa State University, Ames, Iowa 50011, USA*

[2]*Department of Physics and Astronomy and Wright Center for Photovoltaics Innovation and Commercialization, The University of Toledo, Toledo, Ohio 43606, USA*

[3]*Department of Electrical Engineering and Computer Science, Massachusetts Institute of Technology, Cambridge, Massachusetts 02139, USA*

(Received 17 May 2019; revised manuscript received 13 January 2020; accepted 19 February 2020; published 16 March 2020)

The coherence of collective modes, such as phonons and polarons, and their modulation of electronic states is long sought in complex systems, which is a crosscutting issue in photovoltaics and quantum electronics. In photovoltaic cells and lasers based on metal halide perovskites, the presence of polarons, i.e., photocarriers dressed by the macroscopic motion of charged lattice, assisted by terahertz (THz) longitudinal-optical (LO) phonons, has been intensely studied yet is still debated. This may be key for explaining the remarkable properties of the perovskite materials, e.g., defect tolerance, long charge lifetimes, and diffusion lengths. Here we use the intense single-cycle THz pulse with peak electric field up to $E_{\mathrm{THz}} = 1000\ \mathrm{kV/cm}$ to drive coherent polaronic band-edge oscillations at room temperature in $CH_3NH_3PbI_3$ ($MAPbI_3$). We reveal the oscillatory behavior is dominated by a specific quantized lattice vibration mode at $\omega_{\mathrm{LO}} \sim 4\ \mathrm{THz}$, which is both dipole and momentum forbidden. THz-driven coherent polaron dynamics exhibits distinguishing features: room temperature coherent oscillations at ω_{LO} longer than 1 ps in both single crystals and thin films, *mode-selective* modulation of different band-edge states assisted by electron-phonon interaction, and *dynamic mode splitting* at low temperature due to entropy and anharmonicity of organic cations. Our results demonstrate intense THz-driven coherent band-edge modulation is a powerful probe of electron-lattice coupling phenomena and polaronic quantum control in perovskites.

DOI: 10.1103/PhysRevB.101.115125

I. INTRODUCTION

A challenge underlying efficient photoenergy conversion is to protect photocarrier transport from scattering with disorders. These include static disorders, such as defects and grain boundaries [1], and dynamic ones, such as phonons [2,3], polarons [4–11], rapid organic cation fluctuations, and multicarrier Auger excitations [12]. Perovskites have been identified as a model system for understanding and implementing the large *ferroelectric polaron* formation mechanism [5–7] that screens the Coulomb potential of charge carriers for disorder-immune photoconversion and slow electron-hole (e-h) recombination, among other attractive properties [9–11]. In addition to the generic polaronic coupling, or charge coupling to phonons, ubiquitous in polar lattices [13], the large ferroelectric polarons [5] in perovskites are very relevant for shielding photocarrier transport. The mechanism was discussed [5,7] in the context of the polarization cloud assisted by LO phonon-electron interaction, as illustrated in Fig. 1(a). For example, in analogy to ferroelectric materials, the high-frequency LO mode at $\omega_{\mathrm{LO}} \sim 4\ \mathrm{THz}$ [14], both optically dark and momentum forbidden, has been discussed to provide the macroscopic motion of charged lattice and internal electric field to mediate the large polaron formation. Previous studies have gained important insights into e-phonon interaction and polaronic coupling in perovskites using Raman scattering [15] and coherent phonon pumping [16–19]. However, the high-frequency LO modes of ~4 THz thus far are much less observed by ultrafast optical studies, which reveal mostly lower-frequency modes [18,19]. Recently, high-frequency LO phonon dynamics ~3.7 THz was observed via an optical pump and weak terahertz (THz) probe at room temperature [20]. The next major challenge is to explore the LO mode splitting, controlled by temperature, especially for the 4-THz LO photon mode. In addition, ω_{LO} *mode-specific* coherent coupling to the band-edge states relevant for optoelectronic modulator and device applications has not been revealed.

Probing coherent band-edge modulation, assisted by the LO phonon ω_{LO}, and its selective electronic coupling to different bands requires overcoming the challenges of detecting the dynamics of the ω_{LO} mode, an optically dark one at higher center-of-mass momentum K space. It is restricted from commonly used interband optical transition. Yet the challenge can be met by coherent excitation and detection methods driven by an intense single-cycle THz pulse at femtosecond time and THz frequency scales. As illustrated in Fig. 1(a), subcycle acceleration driven by an intense THz electric field is expected to impulsively distort the high-frequency vibrational potential of LO phonons by dynamically generating internal electric field in $CH_3NH_3PbI_3$ ($MAPbI_3$). For example, THz-induced interband coherence has been identified to assist

*jgwang@iastate.edu; jwang@ameslab.gov

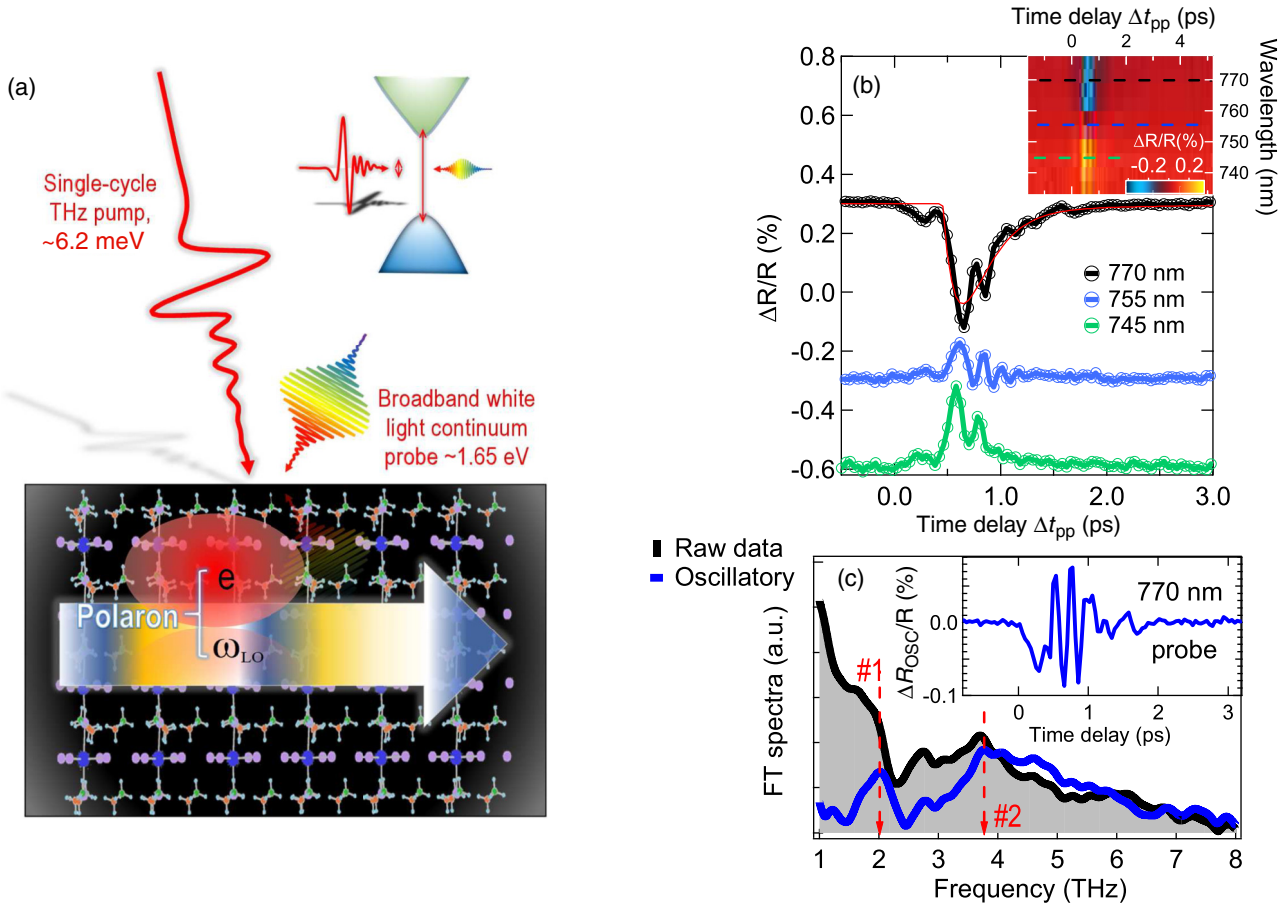

FIG. 1. Room temperature coherent band-edge dynamics in $MAPbI_3$ driven by the intense single-cycle THz electric field pulse. (a) An illustration of polaron formation in $MAPbI_3$ after THz pumping. The ω_{LO}-model specific coupling to band-edge states can be probed by a broadband white-light continuum (inset, top right corner). (b) Three selective $\Delta R/R$ time traces at probe wavelengths of 770 nm (black), 755 nm (blue), and 745 nm (green) induced by THz pump electric field $E_{THz} = 938$ kV/cm at room temperature. The red trace shows the exponential decay component at 770 nm obtained from fitting. Inset: A two-dimensional false-color plot of the full transient spectra as a function of time delay Δt_{pp}. The dashed lines mark the wavelength cut of three $\Delta R/R$ dynamics selected. (c) The Fourier transform (FT) spectra of the $\Delta R/R$ (black) and oscillatory component $\Delta R_{osc}/R$ (blue) at 770 nm. Two pronounced peaks centered at ~4 (arrow 2) and ~2 THz (arrow 1) are marked as red dashed lines. Inset: Raw $\Delta R_{osc}/R$ data in the time domain.

the tunneling of electrons in GaAs [21]. The soft nature of organic-inorganic hybrid perovskite materials makes the ions reside in very shallow minima of the potential energy landscape and can strongly couple to band-edge electronic states, unlike GaAs. In addition, the coherent LO phonons can influence electronic bands depending on their symmetry-dependent selective coupling to the ω_{LO} mode assisted by polaronic coupling. However, the LO-phonon-induced band-edge modulation was not observed in prior THz pumping measurements [22] using a relatively low electric field (~100 kV/cm) that focused on an optical-active, transverse-optical phonon, i.e., the TO mode, at a low frequency of ~1 THz. The megavolt per centimeter THz pumping electric field used here, which is one order of magnitude higher than in prior studies, is required for exciting ω_{LO} coherence and band-edge modulation.

Here we reveal the robust ω_{LO} polaronic quantum oscillation driven by THz pumping at room temperature in both single-crystal and thin-film $MAPbI_3$ samples. This approach allows the observation of a LO mode-selective coupling to different band-edge states. We also reveal LO phonon coherent dynamics, from mode splitting to beating, controlled by temperature due to entropy and anharmonicity of the organic cations. The intense THz-driven quantum beats demonstrated represent a powerful probe for fundamental polaron correlation physics in perovskites, especially with implications that polaron correlation may be critical for perovskites.

II. EXPERIMENTAL RESULTS

Our setup is driven by a 1-kHz Ti:sapphire regenerative amplifier with a 790-nm central wavelength and 40-fs pulse duration [23]. Information on ultrafast THz spectroscopy and general electrodynamics of semiconductors is discussed elsewhere [24–26]. The intense, subpicosecond single-cycle THz pulse [27–32] has a peak electric field up to $E_{THz} =$ 1000 kV/cm and deep-subgap photon energy centered at $\omega_{pump} \sim 1.5$ THz or 6.2 meV. As illustrated in Fig. 1(a), the ground state of $MAPbI_3$ at room temperature exhibits a band gap $E_g \sim 1.51$ eV that is strongly influenced by the orientations and couplings of the MA^+ cations [33,34] and octahedral PbI_6 halide cages [15]. The pump-induced band-edge

coherent oscillations are probed by a delayed, white-light continuum pulse ranging from 735 to 785 nm [inset, Fig. 1(b) a two-dimensional (2D) false-color plot] after the THz pump. Here the wavelength-dependent, transient differential reflectivity $\Delta R/R$ in a $MAPbI_3$ single crystal is recorded as a function of pump-probe delays Δt_{pp} after THz pumping, $E_{THz} = 938\,kV/cm$ at room temperature. The observed $\Delta R/R$ signals exhibit a sign reversal above and below 755 nm that is consistent with the known band gap shift and Pauli blocking nonlinearities from the presence of the transient carrier population. The $\Delta R/R$ dynamics measures free charge carrier decay. Most intriguingly, a pronounced oscillatory behavior is clearly visible and is superimposed on the amplitude decay profile, as shown in Fig. 1(b) for three representative traces at wavelengths of 755 nm (blue), 745 nm (green), and 770 nm (black) selected from the 2D plot (dashed lines). The coherent oscillations persist for at least the first ~2 ps and appear to dephase together with the amplitude decay, e.g., as seen in the exponential decay fitting for the 770-nm trace (red solid line).

Figure 1(c) shows the origin of the periodic oscillations as the LO phonon coherence at ω_{LO} induced by the THz pump. As an example, we isolate an oscillatory component $\Delta R_{osc}/R$ at 770 nm [blue line in the inset of Fig. 1(c)] by removing the best fitted exponential amplitude decay [τ_{exp}, red solid line in Fig. 1(b)] from the $\Delta R/R$ signal [black line in Fig. 1(b)]. The $\Delta R_{osc}/R$ dynamics clearly show quantum beatings of multiple modes. The Fourier transformation (FT) spectra of $\Delta R_{osc}/R$ dynamics display these two modes, one pronounced peak centered at ~4 THz (arrow 2), which matches the LO phonon ω_{LO} frequency [14] that is discussed in the context of the polaron formation [5], and another secondary peak at ~2 THz (arrow 1), which is consistent with the TO phonon mode ω_{TO} seen in ultrafast THz and infrared absorption of $MAPbI_3$ [2,35]. The ω_{LO} mode from coherent dynamics shows a full width at half maximum (FWHM) of ~2 THz [blue line in Fig. 1(c)], which is consistent with the lifetime-limited dephasing of ~1 ps measured in the time domain [black line in Fig. 1(b)]. Note that both the ω_{LO} and ω_{TO} modes (marked by arrows) are also clearly visible in the FT spectra of the $\Delta R/R$ raw data (black line) without removing the amplitude decay component, as shown in Fig. 1(c). The exponential subtraction helps suppress the low-frequency (< 1 THz) background in $\Delta R_{osc}/R$ spectra. Moreover, much stronger nonlinearity is seen using a 10 times higher THz pumping field in comparison to the second-order nonlinearity observed in the previous THz pump study [22]. We emphasize two points below. First, the second-order electroabsorption mechanism dictates $\Delta R/R$ signals are scaled with the square of the incident THz electric field during the pulse. In contrast, the THz pump-induced $\Delta R/R$ signal here cannot be scaled quadratically, as discussed in the Supplemental Material (Fig. S3) [36]. Second, the 4-THz peaks observed do not show any oscillating behavior associated with the electroabsorption mechanism [22]; for example, 770-nm [Fig. 1(c)] and 745-nm (Fig. S4, Supplemental Material) probes show the same behavior.

Note that the ω_{LO} coherence and dephasing times, revealed in the time domain here by the single-cycle intense THz pump, are close to the previous optical pump results that reveal the polaron mode ~3.7-THz temporal oscillation [20] by detecting the differential frequency between the weak THz probe and polaron collective emission. Note that all these results are consistent with the formation time of ~1 ps for large polarons [37]. Polarization dephasing can lead to conversion of LO phonon coherence into a population of polarons associated with the establishment of dynamic screening of Coulomb interactions. This indicates that the correlated electron-lattice interaction may contribute the observed signals.

III. CONTINUOUS WAVELET TRANSFORM AND THEORETICAL ANALYSIS

A. CWT analysis on $\Delta R_{osc}/R$ of single crystal sample at room temperature

We transform the oscillatory component $\Delta R_{osc}/R$ into the time-frequency domain [Fig. 2(a)] and compare it with the THz driving pulse [Fig. 2(b)] in order to further substantiate the observation of the room temperature ω_{LO} polaronic coupling. Figure 2(a) plots the continuous wavelet transforms (CWT chronograms) of $\Delta R_{osc}/R$ at a probe wavelength of 770 nm for Δt_{pp} up to 5 ps (see the Supplemental Material). The distinct ω_{LO} mode is clearly visible in the time-integrated power spectrum (black circles, side panel). In stark contrast to the ω_{LO} quantum oscillations, the THz driving field in Fig. 2(b) exhibits much slower oscillations (red line, top panel) with the spectrum centered at ~6.2 meV or 1.5 THz (green open circles, side panel), far below the ω_{LO} frequency. This excludes the pump electric field oscillation as the origin of $\Delta R_{osc}/R$ coherent dynamics that exhibit the faster ω_{LO} dynamics from the polaronic coherent coupling. Instead, the direct coupling between the THz pump (green shading) and optically active ω_{TO} phonon (black open circles), both located at ~2 THz (arrow 2), gives rise to the infrared active mode seen in Fig. 2(a). In addition, the CWT plot also allows the determination of subcycle buildup of the ω_{LO} mode during the THz pumping with a dephasing time of ~1 ps. Although the dephasing time measured here is in the limit of the THz pump pulse envelope, it should be noted THz pump effects are mostly on the first cycle of the THz pump field instead of the pulse envelope due in part to the strong threshold behavior associated with the tunneling ionization process. In addition, the dephasing time measured by single-cycle THz-driven quantum beats is consistent with the reported subpicosecond polaron formation [20,37] and the rotational correlation time of organic cations [38,39].

Figure 3 demonstrates mode-selective coupling of the ω_{LO} quantum coherence to different band-edge states at room temperature. We examine closely three CWT time-frequency spectra for the band-edge states in Figs. 3(a)–3(c) at probe wavelengths of 745 nm, 755 nm, and 770 nm, respectively, up to $\Delta t_{pp} = 4.9$ ps. These positions are determined by the locations of the positive and negative extrema as well as the zero point of the $\Delta R/R$ transient spectra and do not change with time delays [inset, Fig. 1(b)]. All plots show the notable 4-THz peak but with a distinctly different spectral power intensity indicative of selective coupling to the ω_{LO} coherent lattice oscillation for the different band-edge states. First, stronger 4-THz peaks appear on two sides at the 745- and 770-nm probes, respectively, above [Fig. 3(a)] and below [Fig. 3(c)] the middle 755-nm one. For example, the coupling strength of the 755-nm probe [Fig. 3(b)] at ~4 THz is

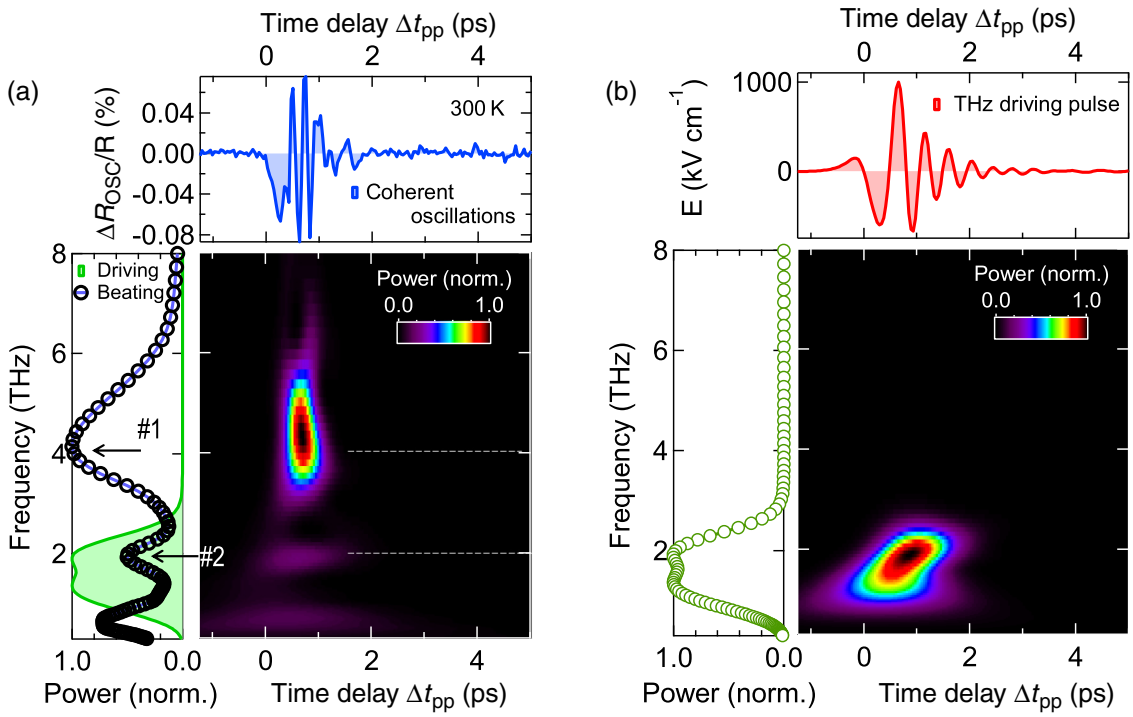

FIG. 2. THz ω_{LO} mode-specific electronic band coupling revealed by intense THz pump-induced quantum beat dynamics and spectra at room temperature. Continuous wavelet transform of (a) the oscillatory component $\Delta R_{osc}/R$ at a probe wavelength of 770 nm and (b) THz driving field. The top panels in (a) and (b) show the $\Delta R_{osc}/R$ (blue line) and THz driving electric field (red line) in the time domain. The time-integrated power spectra from time-frequency analysis of the 770-nm wavelength (black open circles) and THz field (green open circles) are shown on the left in (a) and (b); 2 THz (arrow 2) and 4 THz (arrow 1) are marked in the power spectrum of (a).

suppressed, ~3 times weaker than that of the 770-nm one [Fig. 3(c)]. Second, in comparison with the time-integrated power spectra for electronic states on two sides [Figs. 3(d) and 3(f)], the 755-nm one [Fig. 3(e)] appears broadened, with the FWHM almost 2 times larger, asymmetric towards the high-frequency side due to the appearance of extra spectral weight of ~5 THz (arrow 2). This mode is consistent with the assignment of a MA rotational mode at 165 cm^{-1} for $MAPbI_3$ [14]. Here the 755-nm transition appears to connect more to the organic cation mode, which suppresses the ω_{LO} = 4 THz mode, consistent with our conclusion. Third, the probe wavelengths match very well with three main interband transitions, as shown in Fig. 3(g), i.e., $v_1 \leftrightarrow c_1$, $v_2 \leftrightarrow c_1$, and $v_1 \leftrightarrow c_2$, where c and v are the valence and conduction bands of $MAPbI_3$. Figure 3(g) plots our density functional theory (DFT) calculations (see the Supplemental Material) that show the valence and conduction bands of $MAPbI_3$ near the Fermi level along the $-Y \rightarrow \Gamma \rightarrow Y$ path, with $Y \equiv (0,\ 0.5,\ 0)$ in the conventional basis. The band gap from the DFT band structure calculation with generalized gradient approximation (GGA) for the exchange-correction energy functional is known to be underestimated, with a theoretical value ($E_{c_1} - E_{v_1}$) of 0.64 eV compared with an experimental value of ~1.6 eV. However, the relative positions of valence bands or conduction bands should be quite accurate for $MAPbI_3$, as it is a typical wideband weakly correlated material. The vertical line indicates three electric dipole-allowed interband transitions involving band extrema. Remarkably, the differences in interband transition frequencies, $f_{v_1\leftrightarrow c_2} - f_{v_2\leftrightarrow c_1} =$ 21 meV and $f_{v_2\leftrightarrow c_1} - f_{v_1\leftrightarrow c_1} = 31$ meV, match very well the three probe frequencies of 745 nm, 755 nm, and 770 nm, with spacings of 22 and 32 meV, respectively. This shows that the three wavelengths are probing three band-edge states that can be selectively and periodically modulated. The modulation is assisted by polaronic coupling with ω_{LO} mode and coherence. Such LO phonon mode-selective coupling of the interband transition through polaronic coupling, as demonstrated experimentally, provides an extra knob to engineer the electronic fine structure for applications at room temperature.

Comparing the spectra in Figs. 3(d)–3(f) and the spectral-temporal analysis of the squared THz pump pulse E^2_{THz} in Fig. 3(h), we can rule out the origin of the 4-THz mode being from any second-order electro-optical contribution from THz pumping. First, Fig. 3(h), using the real pump pulse [Fig. 2(b)], shows a spectrum centered at ~3 THz (arrow 3) instead of 4 THz as observed. This is consistent with the fact that the THz pump mostly centers at ~1.5 THz not at 2 THz. Second, different center frequencies and spectral broadenings observed in the integrated power spectra between the side 770 nm [Fig. 3(f)] and the center 755 nm [Fig. 3(e)] cannot be explained by the electro-optical absorption mechanism. Third, we can also rule out the origin of the 4-THz mode being from the electro-optical-type effect from the low-temperature measurement discussed below.

B. CWT analysis on $\Delta R_{osc}/R$ of single crystal sample at 90 K

Distinctly different LO phonon modes emerge at low temperature, signifying the salient roles of entropy and anharmonicity of MA^+ cation rotations. We analyze the influence

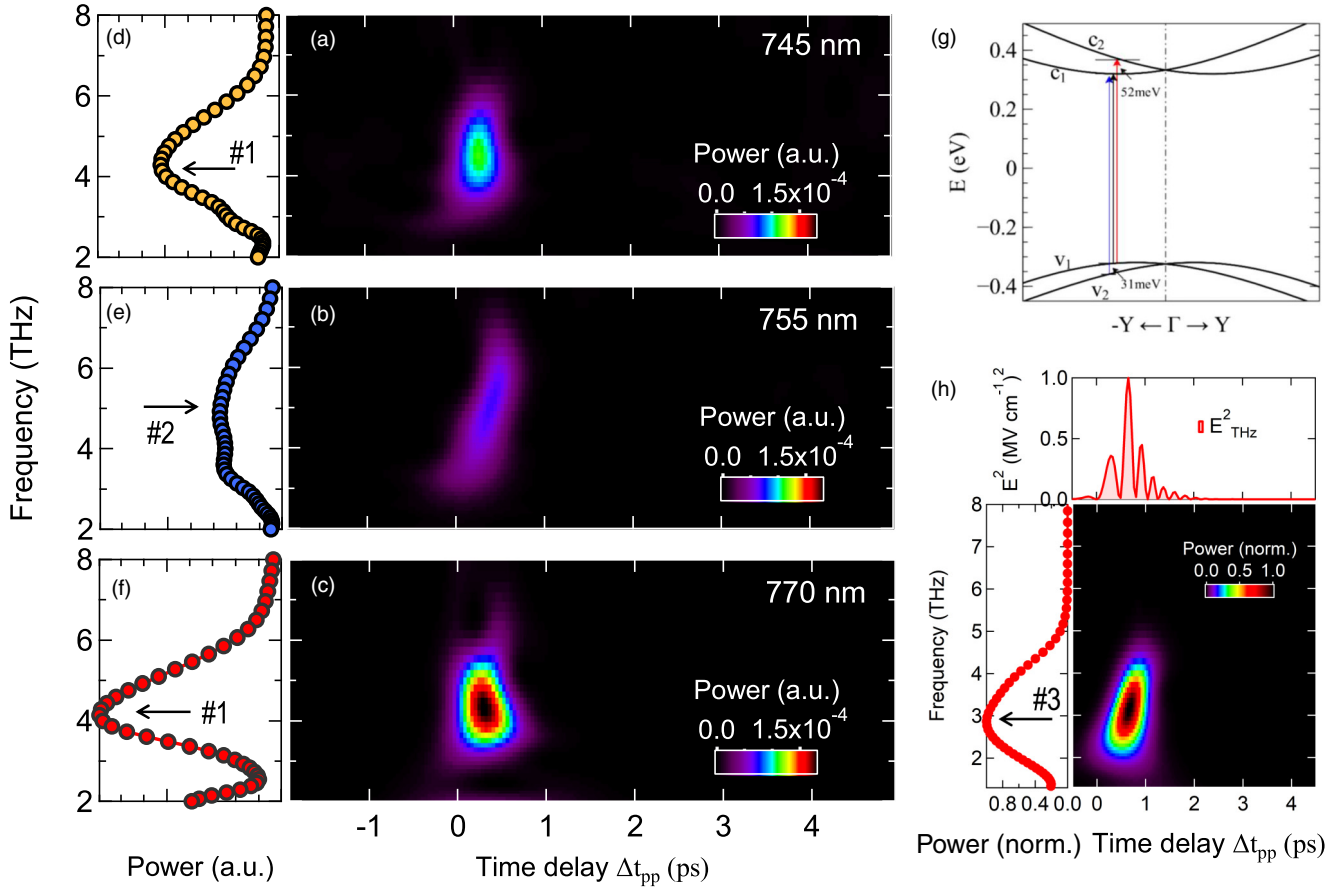

FIG. 3. Selective THz periodic modulation of the band-edge electronic states from their coupling to the ω_{LO} mode-specific coherence and dynamics at room temperature. Continuous wavelet transform of oscillatory components $\Delta R_{osc}/R$ at probe wavelengths of (a) 745, (b) 755, and (c) 770 nm at room temperature. They correspond to the three electric dipole-allowed interband transitions involving band extrema as discussed in the Supplemental Material. (d)–(f) The time-integrated power spectra from time-frequency analysis of the 745-nm (orange solid circles), 755-nm (blue solid circles), and 770-nm (red solid circles) traces. The raw $\Delta R_{osc}/R$ data used in time domain are shown in the Supplemental Material (Fig. S2). (g) Band structure of $MAPbI_3$ calculated at the DFT-GGA level near zero Fermi energy. The Y point is defined as (0, 0.5, 0) in the conventional basis. (h) The time-integrated power spectrum from time-frequency analysis of the squared THz field E^2_{THz} (red circles). Note arrow 1 indicates the 4-THz position, arrow 2 indicates the 5-THz position, and arrow 3 indicates the 3-THz position.

of temperature on the polaron formation in the $MAPbI_3$ single crystal, as shown in Fig. 4(a), by plotting the CWT spectra of the oscillatory component $\Delta R_{osc}/R$ at 90 K (the negative peak position at the probe wavelength of 743 nm). This band has been shown to mostly couple to optically dark ω_{LO} instead of the IR-active MA^+ mode of ∼5 THz shown in Fig. 3(e). In contrast to the dominant ω_{LO} coherent dynamics at room temperature in Fig. 3(d), the quantum beat spectra largely lie below 4 THz centered at $\omega_1 = 1$ THz (arrow 1) and $\omega_2 = 3.3$ THz (arrow 2). These modes match well with the known TO phonons of the PbI_6 perovskite cage [35,40,41]. It is well established that $MAPbI_3$ perovskites go through a first-order phase transition across 160 K, i.e., transforming from the room temperature tetragonal to low-temperature orthorhombic phase. The deformation of the PbI_6 cage below the phase transition temperature strongly restricts the rotation of the organic cation. As a consequence, we can attribute the absence of the 4-THz mode at low temperature to the freeze of organic molecular cation which transfers the spectral weight to low-frequency modes. Most intriguingly, through careful examination of the power spectra in Fig. 4(b), we observed a small peak at higher frequency, lying above 4 THz, centered at $\omega_3 \sim 5$ THz (arrow 3) in both the original (black open circles) and zoomed (red solid line, ×20) traces. This observation can be explained by the phonon splitting of ω_{LO} at 4 THz into two, i.e., the low-frequency ω_2 and high-frequency ω_3 modes due to coupling between the MA^+ cation and the LO phonon. This is in excellent agreement with the recent linear THz absorption spectroscopy study that shows the 4-THz LO mode at room temperature splits into two modes, lying at ∼3.3 and 4.9 THz, in the low-temperature orthorhombic phase [14]. Our results here provide evidence of coherent excitation and detection of these modes. Moreover, comparing the quantum beat spectra at room (Fig. 3) and low [Fig. 4(a)] temperatures, we can rule out the origin of the 4-THz mode being from any second-harmonic-generation contribution from THz pumping, which is expected to be enhanced by decreasing temperature and lack mode splitting.

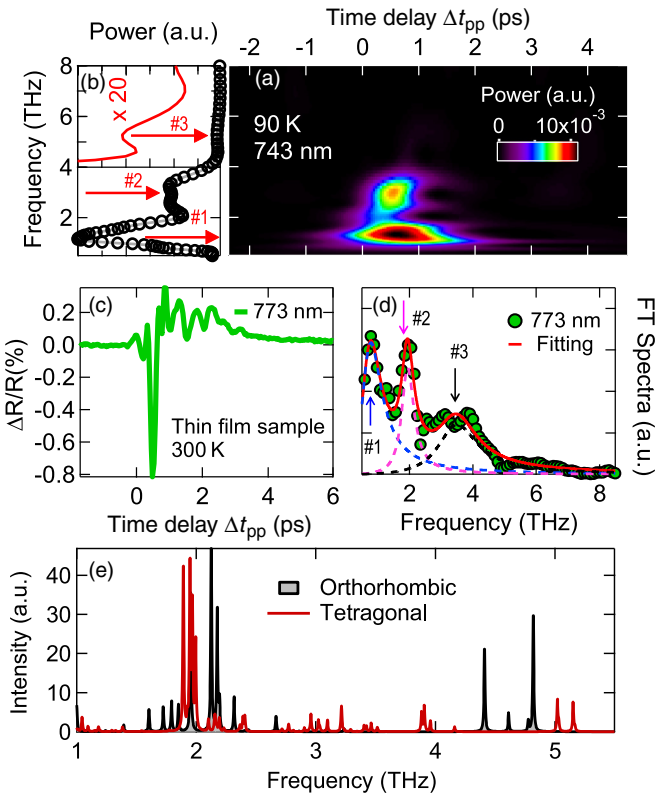

FIG. 4. Dynamic LO mode splitting and dynamics. (a) Continuous wavelet transform of oscillatory component $\Delta R_{osc}/R$ at a probe wavelength of 743 nm at $E_{THz} = 938$ kV/cm and 90 K. (b) Time-integrated power spectrum from the time-frequency analysis of oscillatory component $\Delta R_{osc}/R$ at a probe wavelength of 743 nm, with three peaks "centered" at ~1 THz (arrow 1), 3.3 THz (arrow 2), and 5 THz (arrow 3, red solid line, ×20). (c) A representative $\Delta R/R$ time trace of a $MAPbI_3$ thin film at room temperature induced by $E_{THz} = 938$ kV/cm at a probe wavelength of 773 nm. (d) The Fourier spectrum of the $\Delta R/R$ time trace at a probe wavelength of 773 nm (green). Shown together are the line shape fitting (red line) obtained from three Lorentz oscillators (dashed colored lines) and center frequencies at 0.8 THz (arrow 1, dashed blue line), 1.9 THz (arrow 2, dashed magenta line), and 3.5 THz (arrow 3, dashed black line). (e) Simulated THz phonon spectra convoluted with a 0.01-THz Lorentzian in the tetragonal phase (red line) and orthorhombic phases (black line).

C. LO quantum coherence in thin film sample

We further examine single-cycle THz-driven dynamics in device-relevant $MAPbI_3$ thin-film samples at room temperature. We establish below that the fundamental discovery of LO phonon quantum coherence that has revealed in single crystals so far also appears in perovskite films. Figure 4(c) presents a representative $\Delta R/R$ time trace at a probe wavelength of 773 nm after THz excitation $E_{THz} = 938$ kV/cm at room temperature. Like in single-crystal samples, we observe pronounced quantum oscillations in the time domain lasting a few picoseconds. The FT spectrum of the raw data [green solid circles in Fig. 4(d)] clearly reveals three peaks, marked by arrows, including the high-frequency one at ~4 THz indicative of the THz-driven ω_{LO} quantum coherence. The polycrystalline grains in thin-film samples are likely the main reason for slightly different mode positions and spectral weight distribution [42,43]. The thin-film spectrum can be well fitted by three Lorentz oscillators with center frequencies at 0.8 THz (dashed blue line), 1.9 THz (dashed magenta line), and 3.5 THz (dashed black line). The first two modes are consistent with the infrared-active TO phonon modes commonly seen in thin-film samples [2], while the last one represents the observation of the previously inaccessible ω_{LO} mode that has large polaronic coupling and exists in both the $MAPbI_3$ single crystals and thin films.

D. First-principle modeling of IR spectra

Finally, we discuss the temperature-dependent coupling between electrons and the LO phonon/organic MA cations in different structural phases observed in comparison with the first-principles modeling of IR phonon spectra at different phases controlled by temperature. The tetragonal phase of $MAPbI_3$ allows the fast rotation of the MA cations in the perovskite cage, which causes the dynamic disorder and damped coherent oscillations at high temperature. These are among the most important factors responsible for reduction of the carrier mobility and diffusion length. At the low-temperature orthorhombic phase the cations are restricted, which leads to the characteristic mode splitting of the LO phonon observed in Fig. 4(a). To put this on a strong footing, Fig. 4(e) provides the first-principles modeling of IR phonon spectra at different temperatures. We compare the theoretical zone-center IR phonon spectrum of the sample in the room temperature tetragonal phase with that in the low-temperature orthorhombic phase. Consistent with experiment, the high density of phonon modes close to 4 THz is clearly present at the tetragonal phase. As the system transforms from the tetragonal phase to the orthorhombic phase with decreasing temperature, the spectral weight near 4 THz splits into higher- and lower-frequency modes, driven by the anharmonic phonon-phonon coupling effect through the phase transition. This is consistent with our results from the observed coherent dynamics. At the low-temperature phase, the exciton plays a significant role as the binding energy becomes bigger than the thermal energy. As temperature rises, the exciton binding energy decreases. At room temperature, the exciton becomes irrelevant in this bulk material. The free-carrier (electron/hole)-phonon coupling can form a polaron. The specific phonon modes, especially the 4-THz LO mode, can strongly contribute to the large polaron formation. The simulation reveals the temperature-dependent phonon mode locking and phonon weight transfer in perovskites, which critically depends on phonon-phonon coupling between the perovskite cage and organic cations.

IV. CONCLUSION

In summary, subcycle THz-driven electronic band-edge modulations revealed the coherent LO phonon dynamics and polaron correlation in perovskites. Our results demonstrate this technique is a powerful probe of polarons in perovskites and provide compelling implications towards controlling polaronic correlation. We also reveal mode-selective modulation of electronic states and LO mode splitting that may have far-reaching consequences for other coherently enhanced

phenomena, e.g., the biological light harvesting seemingly assisted by subpicosecond electronic coherence [44] and quantum femtosecond magnetism [45,46].

ACKNOWLEDGMENTS

This work was supported by the US Department of Energy, Office of Basic Energy Science, Division of Materials Sciences and Engineering (Ames Laboratory is operated for the US Department of Energy by Iowa State University under Contract No. DE-AC02-07CH11358). Sample development at the University of Toledo was supported by National Science Foundation Grant No. DMR 1807818. Sample development at the Massachusetts Institute of Technology was supported by the National Science Foundation Graduation Research Fellowship under Grant No. 1122374. The terahertz spectroscopy instrument was supported by National Science Foundation Grant No. EECS 1611454.

[1] Z. Liu, K. C. Bhamu, L. Luo, S. Shah, J.-M. Park, D. Cheng, M. Long, R. Biswas, F. Fungara, R. Shinar, J. Shinar, J. Vela, and J. Wang, MRS Commun. **8**, 961 (2018).

[2] L. Luo, L. Men, Z. Liu, Y. Mudryk, X. Zhao, Y. Yao, J.-M. Park, R. Shinar, J. Shinar, K.-M. Ho, I. E. Perakis, J. Vela, and J. Wang, Nat. Commun. **8**, 15565 (2017).

[3] Z. Liu, C. Vaswani, X. Yang, X. Zhao, Y. Yao, Z. Song, D. Cheng, Y. Shi, L. Luo, D. H. Mudiyanselage, C. Huang, J.-M. Park, J. Zhao, Y. Yan, K.-M. Ho, and J. Wang, arXiv:1905.12373.

[4] P. P. Joshi, S. F. Maehrlein, and X.-Y. Zhu, Adv. Mater. **31**, 1803054 (2019).

[5] D. Cheng, Z. Liu, L. Luo, C. Vaswani, J.-M. Park, Y. Yao, Z. Song, C. Huang, D.-H. Mudiyanselage, R. H. J. Kim, Y. Yan, K.-M. Ho, and J. Wang, J. Chem. Phys. **151**, 244706 (2019).

[6] H. Zhu, K. Miyata, Y. Fu, J. Wang, P. P. Joshi, D. Niesner, K. W. Williams, S. Jin, and X.-Y. Zhu, Science **353**, 1409 (2016).

[7] K. Miyata and X.-Y. Zhu, Nat. Mater. **17**, 379 (2018).

[8] M. Sendber, P. K. Nayak, D. A. Egger, S. Beck, C. Müller, B. Epding, W. Kowalsky, L. Kronik, H. J. Snaith, A. Pucci, and R. L. Lovrinčić, Mater. Horiz. **3**, 613 (2016).

[9] X.-Y. Zhu and V. Podzorov, J. Phys. Chem. Lett. **6**, 4758 (2015).

[10] Y. Chen, H. T. Yi, X. Wu, R. Haroldson, Y. N. Gartstein, Y. I. Rodionov, K. S. Tikhonov, A. Zakhidov, X.-Y. Zhu, and V. Podzorov, Nat. Commun. **7**, 12253 (2016).

[11] F. Zheng and L. Wang, Energy Environ. Sci. **12**, 1219 (2019).

[12] T. M. Brenner, D. A. Egger, L. Kronik, G. Hodes, and D. Cahen, Nat. Rev. Mater. **1**, 15007 (2016).

[13] A. S. Alexandrov, *Polarons in Advanced Materials* (Springer, Dordrecht, 2007).

[14] M. Nagai, T. Tomioka, M. Ashida, M. Hoyano, R. Akashi, Y. Yamada, T. Aharen, and Y. Kanemitsu, Phys. Rev. Lett. **121**, 145506 (2018).

[15] O. Yaffe, Y. Guo, L. Z. Tan, D. A. Egger, T. Hull, C. C. Stoumpos, F. Zheng, T. F. Heinz, L. Kronik, M. G. Kanatzidis, J. S. Owen, A. M. Rappe, M. A. Pimenta, and L. E. Brus, Phys. Rev. Lett. **118**, 136001 (2017).

[16] G. Batignani, G. Fumero, A. R. S. Kandada, G. Cerullo, M. Gandini, C. Ferrante, A. Petrozza, and T. Scopigno, Nat. Commun. **9**, 1971 (2018).

[17] T. Ghosh, S. Aharon, L. Etgar, and S. Ruhman, J. Am. Chem. Soc. **139**, 18262 (2017).

[18] C. Fei, J. S. Sarmiento, and H. Wang, J. Phys. Chem. C **122**, 17035 (2018).

[19] F. Thouin, D. A. Valverde-Chávez, C. Quarti, D. Cortecchia, I. Bargigia, D. Beljonne, A. Petrozza, C. Silva, and A. R. S. Kandada, Nat. Mater. **18**, 349 (2019).

[20] Y. Lan, B. J. Dringoli, D. A. Valverde-Chávez, C. S. Ponseca, Jr., M. Sutton, Y. He, M. G. Kanatzidis, and D. G. Cooke, Sci. Adv. **5**, eaaw5558 (2019).

[21] W. Kuehn, P. Gaal, K. Reimann, M. Woerner, T. Elsaesser, and R. Hey, Phys. Rev. B **82**, 075204 (2010).

[22] H. Kim, J. Hunger, E. Cánovas, M. Karakus, Z. Mics, M. Grechko, D. Turchinovich, S. H. Parekh, and M. Bonn, Nat. Commun. **8**, 687 (2017).

[23] A. Patz, T. Li, S. Ran, R. M. Fernandes, J. Schmalian, S. L. Bud'ko, P. C. Canfield, I. E. Perakis, and J. Wang, Nat. Commun. **5**, 3229 (2014).

[24] X. Yang, X. Zhao, C. Vaswani, C. Sundahl, B. Song, Y. Yao, D. Cheng, Z. Liu, P. P. Orth, M. Mootz, J. H. Kang, I. E. Perakis, C.-Z. Wang, K.-M. Ho, C. B. Eom, and J. Wang, Phys. Rev. B **99**, 094504 (2019).

[25] L. Luo, I. Chatzakis, A. Patz, and J. Wang, Phys. Rev. Lett. **114**, 107402 (2015).

[26] I. Chatzakis, L. Luo, J. Wang, N.-H. Shen, T. Koschny, J. Zhou, and C. M. Soukoulis, Phys. Rev. B **86**, 125110 (2012).

[27] X. Yang, C. Vaswani, C. Sundahl, M. Mootz, P. Gagel, L. Luo, J. H. Kang, P. P. Orth, I. E. Perakis, C. B. Eom, and J. Wang, Nat. Mater. **17**, 586 (2018).

[28] X. Yang, C. Vaswani, C. Sundahl, M. Mootz, L. Luo, J. H. Kang, I. E. Perakis, C. B. Eom, and J. Wang, Nat. Photonics **13**, 707 (2019).

[29] L. Luo, X. Yang, X. Liu, Z. Liu, C. Vaswani, D. Cheng, M. Mootz, X. Zhao, Y. Yao, C.-Z. Wang, K.-M. Ho, I. E. Perakis, M. Dobrowolska, J. K. Furdyna, and J. Wang, Nat. Commun. **10**, 607 (2019).

[30] X. Yang, L. Luo, C. Waswani, X. Zhao, Y. Yao, D. Cheng, Z. Liu, R. H. J. Kim, X. Liu, M. D. Furdyna, J. K. Furdyna, I. E. Perakis, C.-Z. Wang, K.-M. Ho, and J. Wang, npj Quantum Mater. **5**, 13 (2020).

[31] C. Vaswani, C. Sundahl, M. Mootz, D. H. Mudiyanselage, J. H. Kang, X. Yang, D. Cheng, C. Huang, R. H. J. Kim, Z. Liu, L. Luo, I. E. Perakis, C. B. Eom, and J. Wang, arXiv:1912.01676.

[32] X. Yang, L. Luo, M. Mootz, A. Patz, S. L. Bud'ko, P. C. Canfield, I. E. Perakis, and J. Wang, Phys. Rev. Lett. **121**, 267001 (2018).

[33] J. Ma and L.-W. Wang, Nano Lett. **15**, 248 (2015).

[34] A. A. Bakulin, O. Selig, H. J. Bakker, Y. L. A. Rezus, C. Müller, T. Glaser, R. Lovrincic, Z. Sun, Z. Chen, A. Walsh, J. M. Frost, and T. L. C. Jansen, J. Phys. Chem. Lett. **6**, 3663 (2015).

[35] A. M. A. Leguy, A. R. Goñi, J. M. Frost, J. Skelton, F. Brivio, X. Rodríguez-Martínez, O. J. Weber, A. Pallipurath, M. I. Alonso, M. Campoy-Quiles, M. T. Weller, J. Nelson, A.

Walsh, and P. R. F. Barnes, Phys. Chem. Chem. Phys. **18**, 27051 (2016).

[36] See Supplemental Material at http://link.aps.org/supplemental/10.1103/PhysRevB.101.115125 for further discussion of the experiment scheme, data analysis, and theory calculation, which includes Refs. [22,47–52].

[37] S. A. Bretschneider, I. Ivanov, H. I. Wang, K. Miyata, X.-Y. Zhu, and M. Bonn, Adv. Mater. **30**, 1707312 (2018).

[38] N. P. Gallop, O. Selig, G. Giubertoni, H. J. Bakker, Y. L. A. Rezus, J. M. Frost, T. L. C. Jansen, R. Lovrincic, and A. A. Bakulin, J. Phys. Chem. Lett. **9**, 5987 (2018).

[39] G. M. Bernard, R. E. Wasylishen, C. I. Ratcliffe, V. Terskikh, Q. Wu, J. M. Buriak, and T. Hauger, J. Phys. Chem. A **122**, 1560 (2018).

[40] M. A. Pérez-Osorio, R. L. Milot, M. R. Filip, J. B. Patel, L. M. Herz, M. B. Johnston, and F. Giustino, J. Phys. Chem. C **119**, 25703 (2015).

[41] F. Brivio, J. M. Frost, J. M. Skelton, A. J. Jackson, O. J. Weber, M. T. Weller, A. R. Goñi, A. M. A. Leguy, P. R. F. Barnes, and A. Walsh, Phys. Rev. B **92**, 144308 (2015).

[42] O. G. Reid, M. Yang, N. Kopidakis, K. Zhu, and G. Rumbles, ACS Energy Lett. **1**, 561 (2016).

[43] Y. Shao, Y. Fang, T. Li, Q. Wang, Q. Dong, Y. Deng, Y. Yuan, H. Wei, M. Wang, A. Gruverman, J. Shield, and H. Huang, Energy Environ. Sci. **9**, 1752 (2016).

[44] J.-L. Brédas, E. H. Sargent, and G. D. Scholes, Nat. Mater. **16**, 35 (2017).

[45] T. Li, A. Patz, L. Mouchliadis, J. Yan, T. A. Lograsso, I. E. Perakis, and J. Wang, Nature (London) **496**, 69 (2013)

[46] A. Patz, T. Li, X. Liu, J. K. Furdyna, I. E. Perakis, and J. Wang, Phys. Rev. B **91**, 155108 (2015).

[47] M. I. Saidaminov, A. L. Abdelhady, B. Murali, E. Alarousu, V. M. Burlakov, W. Peng, I. Dursun, L. Wang, Y. He, G. Maculan, A. Goriely, T. Wu, O. F. Mohammed, and O. M. Bakr, Nat. Commun. **6**, 7586 (2015).

[48] W. Zhang, S. Pathak, N. Sakai, T. Stergiopoulos, P. K. Nayak, N. K. Noel, A. A. Haghighirad, V. M. Burlakov, D. W. deQuilettes, A. Sadhanala, W. Li, L. Wang, D. S. Ginger, R. H. Friend, and H. J. Snaith, Nat. Commun. **6**, 10030 (2015).

[49] C. C. Stoumpos, C. D. Malliakas, and M. G. Kanatzidis, Inorg. Chem. **52**, 9019 (2013).

[50] Y. Rakita, O. Bar-Elli, E. Meirzadeh, H. Kaslasi, Y. Peleg, G. Hodes, I. Lubomirsky, D. Oron, D. Ehre, and D. Cahen, Proc. Natl. Acad. Sci. U.S.A. **114**, E5504 (2017).

[51] S. G. P. Mahale, B. P. Kore, S. Mukherjee, M. S. Pavan, C. De, S. Ghara, A. Sundaresan, A. Pandey, T. N. Guru Row, and D. D. Sarma, J. Phys. Chem. Lett. **7**, 2412 (2016).

[52] K. Frohna, T. Deshpande, J. Harter, W. Peng, B. A. Barker, J. B. Neaton, S. G. Louie, O. M. Bakr, D. Hsieh, and M. Bernardi, Nat. Commun. **9**, 1829 (2018).